

To view the published open abstract, go to <https://doi.org/10.1029/2022JB024994>

Modelling the Frequency-Dependent Effective Excess Charge Density in Partially Saturated Porous Media

Santiago G. Solazzi¹, Luong Duy Thanh², Kayian Hu³, and Damien Jougnot⁴

¹Institute of Earth Sciences, University of Lausanne, CH-1015 Lausanne, Switzerland

²Thuyloi University, 175 Tay Son, Dong Da, Hanoi, Vietnam

³Department of Geophysics, School of Earth and Space Sciences, Peking University, 100871 Beijing, China

⁴Sorbonne Université, CNRS, EPHE, UMR 7619 METIS, Paris, France

Key Points:

- We present a novel flux-averaging approach to compute the dynamic effective excess charge density in partially saturated porous media.
- The model accounts for the pore size distribution of the medium and permits to estimate the dynamic electrokinetic coupling coefficient.
- The proposed approach has an excellent capability for reproducing previous models and experimental measurements in the literature.

Corresponding author: Santiago G. Solazzi, Santiago.Solazzi@unil.ch

Abstract

In the context of seismoelectric and self-potential surveying, the effective excess charge density and the electrokinetic coupling coefficient are key parameters relating the measured electrical potential and the hydraulic characteristics of the explored porous media. In this work, we present a novel flux averaging approach that permits to estimate the frequency-dependent effective excess charge density in partially saturated porous media. For this, we conceptualize the porous medium as a partially saturated bundle of capillary tubes under oscillatory flux conditions. We account for the pore size distribution (PSD) to determine the capillary-pressure saturation relationship of the corresponding medium, which, in turn, permits to determine the pore scale saturation. We then solve the Navier-Stokes equations within the saturated capillaries and, by means of a flux-averaging procedure, obtain upscaled expressions for: (i) the effective excess charge density, (ii) the effective permeability, and (iii) the electrokinetic coupling coefficient, which are functions of the saturation and the probing frequency. We analyze and explain the characteristics of these functions for three different PSDs: fractal, lognormal, and double lognormal. It is shown that the PSD characteristics have a strong effect on the corresponding electrokinetic response. The proposed flux-averaging approach has an excellent capability for reproducing experimental measurements and models in the literature, which are otherwise based on well-known empirical relationships. The results of this work constitute a useful framework for the interpretation of electrokinetic signals in partially saturated media.

Plain Language Summary

Seismic waves travel throughout the Earth deforming the rocks in their passage. If rocks are porous, permeable, and contain fluids in their pores, as is the case in many geological formations, the wave's passage may induce oscillatory fluid flow. Minerals composing rocks are commonly electrically charged and, thus, the flowing fluid can result in an electrical field. Interestingly, measuring this electrical field at the Earth's surface may permit to characterize the hydromechanical properties of geological formations of interest, motivating the so-called seismoelectric method. The effective excess charge that is mobilized by the fluid motion depends on the frequency content of the wave, and models exist to estimate this dependence in terms of the rock and fluid properties. However, in many scenarios in Earth sciences, rocks contain two immiscible fluid phases, such as,

47 water and air, for which frequency-dependent effective excess charge density models based
48 on pore-scale physics are missing in the literature. In this paper, we derive such a model
49 and show that it is able to reproduce previous estimates and experimental data.

50 **1 Introduction**

51 The remote characterization of partially saturated geological formations using non-
52 invasive techniques remains, to date, a challenging task within the field of applied and
53 environmental geophysics. Given its inherent sensitivity to flow dynamics and pore fluid
54 characteristics, the seismoelectric method can provide highly valuable information for
55 studying this type of environments (Grobbe et al., 2020; Revil et al., 2015). The phys-
56 ical principles upon which seismoelectric prospecting is based on have been used in con-
57 text of groundwater management and remediation (e.g., Dupuis et al., 2007; Han et al.,
58 2004; Monachesi et al., 2018), exploration and production of hydrocarbons (e.g., Revil
59 & Jardani, 2010), and CO₂ geosequestration operations (e.g., Zyserman et al., 2015). Novel
60 approaches addressing the complex processes behind the seismic-to-electric conversion
61 are of great interest, as they may help to better interpret seismoelectrical signatures in
62 partially saturated environments.

63 The seismic-to-electric conversion occurs when a seismic wave propagates through
64 a fluid saturated and charged porous medium, generating fluid displacements relative to
65 the pore walls (e.g., Pride, 1994). Given that, in general, the surfaces of wet minerals
66 composing porous rocks are electrically charged, an electrical double layer (EDL) arises
67 within the saturating pore fluid which counterbalances the net charge present in the min-
68 erals. The EDL contains an excess of charge that is distributed in two layers: (i) the Stern
69 layer, where charges are virtually immobile, and (ii) the diffuse layer, where charges have
70 the capacity to move freely (e.g., Revil & Mahardika, 2013). Whenever a passing seis-
71 mic wavefield induces flow, the excess charge located in the diffuse layer is dragged into
72 motion, generating a streaming current which, in turn, results in an electrical potential
73 distribution. The associated electrical field, which can be surveyed remotely, either at
74 the Earth's surface or at boreholes, contains valuable information regarding the hydrome-
75 chanical properties of the probed geological formation. Laboratory and borehole mea-
76 surements evidence that seismoelectric signals are sensitive to, for example, the poros-
77 ity and permeability of porous media (e.g., Zhu et al., 2008; Wang et al., 2015), and to
78 salt concentration and dielectric permittivity of the saturating fluid (e.g., Zhu & Tok-

soz, 2013; Garambois & Dietrich, 2001). Seismoelectric signals measured in surface surveying or borehole logging have been used, for example, to explore earthquake rupture characteristics (e.g., Gao et al., 2016), to identify formation boundaries associated with lithological changes (e.g., Butler, 1996; Garambois & Dietrich, 2001), and to detect saturation changes in permeable geological formations (e.g., Thompson & Gist, 1993).

The seismoelectric conversion is traditionally modeled using of the electrokinetic coupling coefficient $C_{EK}(\omega)$, which is a frequency-dependent parameter relating the electrical potential difference (i.e., the electrical field) and the pore fluid pressure gradient driving the fluid flow. In this context, the most frequently used models to estimate $C_{EK}(\omega)$ are based on the works of: (i) Pride (1994) and (ii) Packard (1953). On the one hand, Pride’s (1994) model is based on volume averaging principles and on the dynamic permeability model proposed by Johnson et al. (1987). On the other hand, the pioneering model of Packard (1953) considers a capillary tube of a unique radius and computes the streaming potential difference associated with an oscillatory flux. This model has been widely applied to porous media with a certain success (e.g., Reppert, 2001). Recently, Thanh et al. (2021) extended the work of Packard (1953) to take into account different pore size distributions (PSD), thus showing the effects of the porous structure on $C_{EK}(\omega)$. An alternative approach for studying the seismoelectric conversion is to compute the excess charges that are effectively dragged in the diffuse layer, that is, the effective excess charge density \hat{Q}_ν , which can be subsequently used to estimate C_{EK} (e.g., Jackson, 2010; Jougnot et al., 2012; Revil & Mahardika, 2013). In the literature, many studies were performed considering this effective excess charge density but neglecting its frequency-dependence, that is, considering its low-frequency limit (e.g., Jougnot et al., 2013; Rosas-Carbalajal et al., 2020). Recently, Jougnot and Solazzi (2021) extended the definition of \hat{Q}_ν to the entire frequency range $\hat{Q}_\nu(\omega)$, thus allowing to compute $C_{EK}(\omega)$. For this, the authors integrated the charges that are effectively dragged along individual pores across the probed medium, accounting for inertial effects associated with the oscillatory pressure forcing generated by a passing seismic wavefield. We remark that the latter work reconciled both Pride (1994) and Packard (1953) approaches by integrating flux averaging principles and the dynamic permeability concept. All of the above described works deal with the frequency-dependence of the coupling coefficient $C_{EK}(\omega)$ and/or the effective excess charge $\hat{Q}_\nu(\omega)$ under fully saturated conditions and, thus, modifications are needed if one wishes to employ the corresponding approaches in partially saturated porous media.

112 Evidence indicates conclusively that water content variations in porous media have
 113 preminent effects on the associated seismoelectric signatures (e.g., Bordes et al., 2015;
 114 Zyserman et al., 2017). When exploring partially saturated media using the seismoelec-
 115 tric method, one can also use either the coupling coefficient C_{EK} and/or the effective
 116 excess charge density \hat{Q}_ν to study the electro-kinetic process. Warden et al. (2013) ex-
 117 tended the electrokinetic coupling coefficient $C_{EK}(S_w)$ definition to address partially sat-
 118 urated conditions, highlighting the key influence of water content on the seismoelectric
 119 conversion. The coupling coefficient in partially saturated conditions is generally obtained
 120 by scaling its fully saturated counterpart by the wetting phase saturation (Bordes et al.,
 121 2015; Revil & Mahardika, 2013; Warden et al., 2013; Zyserman et al., 2017). Later on,
 122 Revil and Mahardika (2013) proposed a simple model to compute the saturation- and
 123 frequency-dependent effective excess charge density of partially saturated porous media
 124 $\hat{Q}_\nu(\omega, S_w)$ and through it, to estimate $C_{EK}(\omega, S_w)$. For this, Revil and Mahardika (2013)
 125 rely on concept of dynamic permeability, using a Debye approximation, and on empiric
 126 and broadly used scaling laws, thus extending the approach proposed by Pride (1994)
 127 to partially saturated media. As far as we know, to date, a model deriving the saturation-
 128 and frequency-dependent effective excess charge density $\hat{Q}_\nu(\omega, S_w)$ from first principles,
 129 that is, from flux averaging the pore scale physics, is lacking in the specific literature.
 130 Such derivation is of fundamental importance, as it would permit to: (i) couple flux, elec-
 131 trokinetic properties, and the pore size distribution characteristics of porous media; (ii)
 132 validate the approach proposed by Revil and Mahardika (2013).

133 In this work, we propose a novel flux averaging approach to estimate the effective
 134 excess charge density as a function of saturation and frequency $\hat{Q}_\nu(\omega, S_w)$. The paper
 135 is structured as follows. First, we resume the theory behind the frequency-dependence
 136 of the effective excess charge density $\hat{Q}_\nu(\omega)$ and other parameters, such as, the dynamic
 137 permeability $\kappa(\omega)$ and the electrokinetic coupling coefficient $C_{EK}(\omega)$. Then, we propose
 138 a model to account for different saturation states in the latter. We evaluate the satu-
 139 ration and frequency response of the medium considering fractal, lognormal, and dou-
 140 ble lognormal PSDs. Finally, we compare the proposed approach with the model pro-
 141 posed by Revil and Mahardika (2013) and with published experimental data.

2 Theory

In this section, we resume the theory of dynamic (frequency-dependent) permeability and effective excess charge density in fully saturated media. Then, we extend these definitions to the partially saturated state, considering that the pore fluids are immiscible and that their distribution throughout the pore space is determined by capillary forces. In the case of the dynamic permeability, we follow the work of Solazzi et al. (2020), who derived frequency- and saturation-dependent effective permeability estimates in partially saturated porous media.

2.1 Frequency-Dependent Effective Excess Charge Density in Fully Saturated Media

2.1.1 Fluid Flow and Dynamic Permeability

Let us consider a cylindrical representative elementary volume (REV) of a porous material of length L (m) and radius R_{REV} (m). We conceptualize the fluid flow of a single phase across the REV using a bundle of aligned capillary tubes, oriented along the axis of the cylindrical REV, comprising radii R (m) whose sizes vary from R_{min} to R_{max} . The pore-size distribution (PSD) is such that the number of capillaries with radii between R and $R+dR$ is given by $f(R)dR$. Note that this conceptualization of a porous medium under fluid flow is based on similar concepts as the classic model of Kozeny (1927), which is broadly used in permeable soils (e.g., Mavko et al., 2009). Let us also consider that an incompressible Newtonian fluid characterized by a shear viscosity η (Pa.s) and density ρ (kg/m³) saturates the porous medium, whose solid matrix is assumed to be rigid (Johnson et al., 1987). Note that the fluid incompressibility assumption is valid at the pore scale as long as the wavelengths of possible acoustic waves traveling in the fluid are much larger than the characteristic pore size (Johnson et al., 1987; Zhou & Sheng, 1989). Finally, we consider that the fluid flow within the pore space is of laminar-type associated with a small Reynold's number (Auriault et al., 1985; Smeulders et al., 1992).

The REV structure is then subjected to an oscillatory pore fluid pressure difference $\Delta\hat{p} = \Delta p e^{-i\omega t}$ (Pa) along its axis., with ω denoting the angular frequency (rad/s). Solving the incompressible Navier-Stokes equations under the assumptions mentioned above, the fluid velocity v^f (m/s) in a capillary of internal radius $0 \leq r \leq R$ responds

172 to (Solazzi et al., 2020)

$$173 \quad v^f(r, \omega) = -\frac{1}{\tau\eta k^2} \left[\frac{J_0(kr)}{J_0(kR)} - 1 \right] \frac{\Delta p}{L}, \quad (1)$$

174 where $k^2 = i\omega\rho/\eta$ and J_ν are Bessel functions of the first kind of order ν . The tortu-
 175 osity is given by $\tau = l^*/L$, where l^* is the actual flow path length. Note that we have
 176 dropped the harmonic term $e^{-i\omega t}$ for ease of notation. Integrating equation (1) over the
 177 cross-sectional area of the pore, the corresponding volumetric flow rate (m^3/s) through
 178 a single capillary is given by (e.g., Johnson et al., 1987)

$$179 \quad q(R, \omega) = -\frac{\pi R^2}{\tau\eta k^2} \left[\frac{2}{kR} \frac{J_1(kR)}{J_0(kR)} - 1 \right] \frac{\Delta p}{L}. \quad (2)$$

180 The volumetric flow rate $Q_{\text{flow}}^{\text{sat}}$ (m^3/s) at the fully-saturated REV-scale can be obtained
 181 by integrating equation (2) over the entire range of pore sizes within the REV

$$182 \quad Q_{\text{flow}}^{\text{sat}} = \int_{R_{\text{min}}}^{R_{\text{max}}} q(R, \omega) f(R) dR. \quad (3)$$

183 The effective Darcy velocity at the REV scale v^{sat} (m/s) is obtained by scaling the vol-
 184 umetric flow rate by the corresponding cross-sectional area, that is, $v^{\text{sat}} = Q_{\text{flow}}^{\text{sat}}/\pi R_{\text{REV}}^2$.

185 If one increases the frequency of the oscillatory pressure forcing, a transition from
 186 viscous- to inertia-dominated flow occurs. For a given critical angular frequency ω_c , the
 187 viscous skin depth $\delta = \sqrt{2\eta/\rho\omega}$ (m) becomes comparable to the radii of the largest sat-
 188 urated pores (Johnson et al., 1987)

$$189 \quad \omega_c \simeq \frac{2\eta}{\check{R}^2 \rho}, \quad (4)$$

190 with \check{R} being the characteristic radius of the saturated porous medium. For frequencies
 191 higher than ω_c the fluid motion becomes viscously decoupled. In this context, the fluid
 192 flow and the underlying fluid pressure forcing become out of phase and the fluid flow am-
 193 plitude decreases.

194 The dynamic (frequency-dependent) permeability $\kappa(\omega)$ (m^2) is then computed us-
 195 ing Darcy's law, that is, relating the fluid flow and the pressure gradient along the REV
 196 (Solazzi et al., 2020)

$$197 \quad \kappa(\omega) = \frac{1}{\tau R_{\text{REV}}^2 k^2} \int_{R_{\text{min}}}^{R_{\text{max}}} \left[\frac{2}{kR} \frac{J_1(kR)}{J_0(kR)} - 1 \right] R^2 f(R) dR. \quad (5)$$

198 Equation (5) can be solved numerically provided that $f(R)$, R_{min} , and R_{max} are known.
 199 One of the consequences of equation (5) is that the pore size distribution has an impact
 200 on the dynamic permeability characteristics, such as, the value of ω_c (Solazzi et al., 2020).

201 We remark that, following a different approach than the one proposed by Solazzi et al.
 202 (2020), Li et al. (2021) arrived to the very same conclusion.

203 The low-frequency limit of equation (5) is the (Poiseuille-type) permeability of the
 204 medium (Blunt, 2017)

$$205 \quad \kappa^0 = \frac{1}{\tau 8 R_{\text{REV}}^2} \int_{R_{\text{min}}}^{R_{\text{max}}} R^4 f(R) \, dR. \quad (6)$$

206 **2.1.2 Effective Excess Charge Density**

207 Let us now consider that the capillaries of the previously described porous medium
 208 are saturated by a binary symmetric electrolyte (e.g., NaCl) with ionic concentration C_i^w
 209 (mol m⁻³) and valence $z_i = \pm 1$, with i denoting the considered ion. Minerals compos-
 210 ing the pore walls of rocks normally exhibit surface charges when in contact with wa-
 211 ter. As an example, silicate and aluminosilicate minerals present negative charges un-
 212 der natural conditions. Let us then denote co-ions the ions that present the same charge
 213 as the minerals constituting the pore walls (e.g., Cl⁻) and, counter-ions those charged
 214 with an opposite valence (e.g., Na⁺). For the system to be electrically neutral, surface
 215 charges are balanced by an excess charge in the pore water. The latter are distributed
 216 in the EDL. Within the EDL, the diffuse layer comprises co-ions and counter-ions that
 217 are able to move and, also, is characterized by a net excess of charge. Hereafter we con-
 218 sider that the shear plane, that is, the plane that separates the stationary fluid and the
 219 moving fluid, corresponds to the interface between the Stern layer and the diffuse layer.
 220 The electrical potential along this plane is referred to as Zeta potential.

221 The distribution of the excess charges in the diffuse layer within a single capillary
 222 is governed by the Poisson-Boltzmann equation

$$223 \quad \nabla^2 \varphi(r) = -\frac{\bar{Q}_\nu(r)}{\varepsilon_r \varepsilon_0}, \quad (7)$$

224 where $\varphi(r)$ (V) is the electric potential and $\bar{Q}_\nu(r)$ (C m⁻³) is the excess charge density
 225 in the liquid at a distance $0 \leq r \leq R$ from the pore-centre. The relative permittivity
 226 of the fluid and the dielectric permittivity of vacuum are given by ε_r and $\varepsilon_0 = 8.854 \times$
 227 10^{-12} F m⁻¹, respectively. Under the above conditions, the effective charge density re-
 228 sponds to (e.g., Jougnot et al., 2012)

$$229 \quad \bar{Q}_\nu(r) = N_A e_0 C_{NaCl}^w \left[e^{\left(-\frac{e_0 \varphi(r)}{k_B T}\right)} - e^{\left(\frac{e_0 \varphi(r)}{k_B T}\right)} \right]. \quad (8)$$

230 Generally, equation (7) is solved assuming: (i) a Debye-Hückel linear approximation, that
 231 is, $e_0\varphi(r)/k_B T \ll 1$; (ii) that the pore size is considerably larger than thickness of the
 232 double layer. In this context, the two exponential terms in Eq. (8) can be expressed through
 233 the sinh function and, then, one can make use of the fact that for sufficiently small ar-
 234 guments the sinh function tends to its corresponding argument, that is, $\sinh [e_0\varphi(r)/k_B T] \simeq$
 235 $e_0\varphi(r)/k_B T$. Consequently, the electric potential is given by

$$236 \quad \varphi(r) = \zeta e^{\frac{r-R}{l_D}}, \quad (9)$$

237 where l_D is the Debye length characterizing the electrical double layer thickness given
 238 by

$$239 \quad l_D = \sqrt{\frac{\varepsilon_0 \varepsilon_r k_B T}{2 N_A e_0^2 C_{NaCl}^w}}. \quad (10)$$

240 The dependence of the ζ potential on the ionic concentration is hereby estimated follow-
 241 ing (Pride & Morgan, 1991)

$$242 \quad \zeta(C_{NaCl}^w) = a + b \log_{10}(C_{NaCl}^w). \quad (11)$$

243 The fitting parameters a and b are taken as $a = -6.43$ mV and $b = 20.85$ mV, as es-
 244 timated by (Jaafar et al., 2009) for NaCl brine and silicate-based materials.

245 In this context, the effective excess charge density \hat{Q}_ν^R carried by the water flow in
 246 a single capillary of radius R responds to (Jougnot & Solazzi, 2021)

$$247 \quad \hat{Q}_\nu^R(\omega) = \frac{\int_0^R \bar{Q}_\nu(r) v^f(r, \omega) r dr}{\int_0^R v^f(r, \omega) r dr}. \quad (12)$$

248 The effective excess charge density \hat{Q}_ν^R is different from the simple excess charge den-
 249 sity \bar{Q}_ν , since \hat{Q}_ν^R is the excess charge that is effectively dragged by the water flow, which
 250 is smaller than the total amount of excess charge present in the diffuse layer ($\bar{Q}_\nu : \bar{Q}_\nu \gg$
 251 \hat{Q}_ν^R). For further details on this particular topic, we refer the readers to the discussion
 252 sections of Jougnot et al. (2019, 2020).

253 The effective excess charge carried by the water flow in the fully saturated REV
 254 can be obtained by integrating $\hat{Q}_\nu^R(\omega)$, weighted by the corresponding fluxes, over the
 255 entire range of pore sizes

$$256 \quad \hat{Q}_\nu^{\text{sat,REV}}(\omega) = \frac{\int_{R_{\min}}^{R_{\max}} \hat{Q}_\nu^R(\omega) q(R, \omega) f(R) dR}{\int_{R_{\min}}^{R_{\max}} q(R, \omega) f(R) dR}, \quad (13)$$

257 where $q(R, \omega)$ is the volumetric flow rate through a single capillary of radius R given by
 258 equation (3). We remark that the supra-index “sat” denotes that the medium is fully

259 saturated and helps to discriminate this parameter from its partially saturated counter-
 260 part, defined in the next subsection of this paper.

261 Finally, based on the above described expressions, it is possible to define a relative
 262 excess charge density (Jougnot & Solazzi, 2021),

$$263 \quad \hat{Q}_\nu^{\text{sat,rel}}(\omega) = \frac{\hat{Q}_\nu^{\text{sat,REV}}(\omega)}{\hat{Q}_\nu^{\text{sat},0}}, \quad (14)$$

264 where $\hat{Q}_\nu^{\text{sat},0} = \lim_{\omega \rightarrow 0} \hat{Q}_\nu^{\text{sat,REV}}(\omega)$ is the steady-state (low frequency) excess charge
 265 density of the fully saturated medium.

266 *2.1.3 Electrokinetic Coupling Coefficient*

267 At the REV scale, the electrokinetic coupling is usually quantified by means of the
 268 electrokinetic coupling coefficient (e.g., Jaafar et al., 2009)

$$269 \quad C_{EK}(\omega) = \left(\frac{\partial \varphi}{\partial p} \right)_{\mathbf{J}=\mathbf{0}, \ddot{\mathbf{u}}_s=0} = \frac{\Delta V}{\Delta p}, \quad (15)$$

270 which is the ratio of the electrical potential difference ΔV and the pressure difference
 271 Δp measured at the boundaries of a probed rock sample in the absence of total current
 272 densities $\mathbf{J} = \mathbf{0}$ and solid frame accelerations $\ddot{\mathbf{u}}_s = 0$. Through a simple variable change,
 273 the frequency dependent coupling coefficient for a fully saturated medium can be expressed
 274 as (e.g., Jougnot et al., 2020; Jougnot & Solazzi, 2021; Revil & Mahardika, 2013)

$$275 \quad C_{EK}^{\text{sat}}(\omega) = - \frac{\hat{Q}_\nu^{\text{sat,REV}}(\omega) \kappa(\omega)}{\eta_w \sigma^{\text{sat}}(\omega)}, \quad (16)$$

276 where $\kappa_w(\omega)$ and $\hat{Q}_\nu^{\text{sat,REV}}(\omega)$ respond to equations (5) and (13), respectively. We re-
 277 mark here that the electrical conductivity $\sigma^{\text{sat}}(\omega)$ may, as well, present a frequency de-
 278 pendence. For a detailed derivation of equation (16), we refer the reader to, for exam-
 279 ple, the work of Revil and Mahardika (2013) (specifically to equations 34 to 38). Note
 280 that, for steady-state conditions (low-frequency limit), Jougnot et al. (2019) showed that
 281 this equation is valid for any kind of pore space geometry (pore shape and connectiv-
 282 ity) and that the geometrical information is carried through the permeability. In this sense,
 283 as long as the thin double layer assumption is respected, permeability effects are can-
 284 celled in the coupling coefficient as the effective excess charge density depends on the
 285 inverse of the permeability (see discussion in Jougnot et al. (2019, 2020)). However, such
 286 simplification does not hold for the whole frequency range (e.g., Jougnot & Solazzi, 2021),
 287 as the relationship between permeability and effective excess charge density is more com-
 288 plex when considering frequency-dependent effects (see equation 13).

289 The relative electrokinetic coupling coefficient can be expressed as (Jougnot & So-
290 lazzi, 2021)

$$291 \quad C_{EK}^{\text{sat, rel}}(\omega) = \frac{C_{EK}^{\text{sat}}(\omega)}{C_{EK}^{\text{sat}, 0}}, \quad (17)$$

292 where $C_{EK}^{\text{sat}, 0} = \lim_{\omega \rightarrow 0} C_{EK}^{\text{sat}}(\omega)$ is the steady-state electrokinetic coupling coefficient
293 of the fully saturated medium.

294 **2.2 Frequency-Dependent Effective Excess Charge Density in Partially** 295 **Saturated Media**

296 *2.2.1 Fluid Flow and Effective Dynamic Permeability*

297 In the context of fluid flow in partially saturated porous media, the wetting phase
298 flows through a fraction of the corresponding medium. Thus, Darcy's equation in partially-
299 saturated media is (e.g., Bear, 1972)

$$300 \quad \mathbf{v}_w = -\frac{\kappa^{\text{eff}}}{\eta_w} \nabla p_w. \quad (18)$$

301 In equation (18), \mathbf{v}_w is Darcy's velocity of the wetting phase, κ^{eff} is the effective perme-
302 ability of the wetting phase which responds to

$$303 \quad \kappa^{\text{eff}}(\omega) = \kappa(\omega) \kappa_w^{\text{rel}}(p_c, \omega), \quad (19)$$

304 with $\kappa_w^{\text{rel}}(p_c, \omega)$ denoting the frequency dependent relative permeability of the wetting
305 phase, and p_c (Pa) the capillary pressure.

306 The Young-Laplace equation permits us to obtain the capillary pressure in partially
307 saturated capillary of radius R_p (e.g., Bear, 1972)

$$308 \quad p_c = \frac{2\gamma \cos(\beta)}{R_p}, \quad (20)$$

309 where γ (N/m) is the interfacial tension and β (rad) is the contact angle between the
310 solid walls and the saturating immiscible fluid phases. At the REV scale, p_c normally
311 presents a functional relationship with the saturation of the medium (e.g., Van Genuchten,
312 1980; Brooks & Corey, 1964). If the medium is at capillary pressure equilibrium, all cap-
313 illaries presenting radii $R > R_p(p_c) = \frac{2\gamma \cos(\beta)}{p_c}$ are to be saturated by the non-wetting
314 phase (e.g., Mualem, 1976) and those satisfying $R \leq R_p(p_c)$ are to be saturated by the
315 wetting phase. It is then straightforward to compute the associated effective wetting phase
316 saturation $S_{\text{ew}}(p_c)$, which yields (e.g., Blunt, 2017)

$$317 \quad S_{\text{ew}}(p_c) = \frac{\int_{R_{\min}}^{R_p(p_c)} R^2 f(R) dR}{\int_{R_{\min}}^{R_{\max}} R^2 f(R) dR}, \quad \text{with } p_{c, \min} \leq p_c \leq p_{c, \max}, \quad (21)$$

318 with $p_{c,\max} = 2\gamma\cos\beta/R_{\min}$ and $p_{c,\min} = 2\gamma\cos\beta/R_{\max}$. When capillary pressures are
 319 such that $p_c < p_{c,\min}$ we have $S_{we} = 1$ and, alternatively, when $p_c > p_{c,\max}$ we have
 320 $S_{we} = 0$. We remark that equation (21) assumes that the partially saturated porous
 321 medium is characterized by fully connected fluid phases, which saturate particular sub-
 322 sets of the probed porous medium (Blunt, 2017). The effective saturation S_{we} is related
 323 to the total S_w saturation by $S_w = S_{we}(1 - S_{wr}) + S_{wr}$, with S_{wr} denoting the wetting
 324 fluid residual saturation.

325 The effective volumetric flow rates for the wetting phase can be obtained by inte-
 326 grating equation (3) between R_{\min} and $R_p(p_c)$, respectively. Then, employing equation
 327 (18), the frequency-dependent dynamic effective permeability for the wetting phase is
 328 (Solazzi et al., 2020)

$$329 \quad \kappa_w^{\text{eff}}(p_c, \omega) = \frac{1}{\tau R_{\text{REV}}^2 k_w^2} \int_{R_{\min}}^{R_p(p_c)} \left[\frac{2}{k_w R} \frac{J_1(k_w R)}{J_0(k_w R)} - 1 \right] R^2 f(R) dR, \quad (22)$$

330 where $k_w^2 = i\omega\rho_w/\eta_w$. Note that equation (22) is the extension of equation (5) to par-
 331 tially saturated media, as $p_c = p_c(S_w)$. As expected, in the low-frequency limit, this
 332 expression converge to its Poiseuille-type counterpart (e.g., Blunt, 2017)

$$333 \quad \kappa_w^{\text{eff},0}(p_c) = \frac{1}{\tau 8 R_{\text{REV}}^2} \int_{R_{\min}}^{R_p(p_c)} R^4 f(R) dR. \quad (23)$$

334 Please note that, in the derivation of equation (22), a no-slip condition is assumed
 335 to prevail at the interface between the saturating fluid and the pore walls. In presence
 336 of a non-negligible flow velocity at the fluid-pore wall boundary (slip condition), which
 337 may arise due to wettability effects, the dynamic permeability estimates (Li et al., 2020)
 338 and the electrokinetic response of the medium (Collini & Jackson, 2022) are expected
 339 to change. Such boundary effects are, however, beyond the scope of this work.

340 **2.2.2 Effective Excess Charge Density**

341 The effective excess charge carried by the water flow a the partially saturated medium
 342 is then obtained by integrating the excess charge along the pores that are effectively sat-
 343 urated with water for a given capillary pressure p_c , weighted by the corresponding flow
 344 rates

$$345 \quad \hat{Q}_\nu^{\text{REV}}(p_c, \omega) = \frac{\int_{R_{\min}}^{R_p(p_c)} \hat{Q}_\nu^R(\omega) q(R, \omega) f(R) dR}{\int_{R_{\min}}^{R_p(p_c)} q(R, \omega) f(R) dR}. \quad (24)$$

346 Note that since the capillary pressure p_c is related to the water saturation S_w , we con-
 347 sider $\hat{Q}_\nu^{\text{REV}}(p_c(S_w), \omega) \equiv \hat{Q}_\nu^{\text{REV}}(S_w, \omega)$, without loss of generality.

348 Notably, it is possible to define a frequency- and saturation-dependent relative ex-
 349 cess charge density

$$350 \hat{Q}_\nu^{\text{rel}}(S_w, \omega) = \frac{\hat{Q}_\nu^{\text{REV}}(S_w, \omega)}{\hat{Q}_\nu^0(S_w)}, \quad (25)$$

351 where $\hat{Q}_\nu^0(S_w) = \lim_{\omega \rightarrow 0} \hat{Q}_\nu(S_w, \omega)$.

352 **2.2.3 Electrokinetic Coupling Coefficient**

353 By means of the above defined parameters, we extend the dynamic electrokinetic
 354 coupling definition to partially saturated conditions as (Revil & Mahardika, 2013)

$$355 C_{EK}(S_w, \omega) = -\frac{\hat{Q}_\nu^{\text{REV}}(S_w, \omega) \kappa^{\text{eff}}(S_w, \omega)}{\eta_w \sigma(S_w, \omega)}, \quad (26)$$

356 where $\kappa^{\text{eff}}(S_w, \omega)$ and $\hat{Q}_\nu^{\text{REV}}(S_w, \omega)$ respond to equations (22) and (24), respectively. The
 357 electrical conductivity (S/m), in its low-frequency limit, responds to (Waxman & Smits,
 358 1968)

$$359 \sigma^0(S_w) = \frac{S_w^n}{F} \left(\sigma_w + \frac{\sigma_s}{S_w} \right), \quad (27)$$

360 where σ_s (S/m) is the surface conductivity, $F = \tau/\phi$ is the formation factor, and n the
 361 second Archie's coefficient. Even though the electrical conductivity can be considered
 362 as frequency dependent, for simplicity, we hereafter consider $\sigma(S_w, \omega) \approx \sigma^0(S_w)$. For
 363 more information about the frequency dependence of the electrical conductivity, we re-
 364 fer the readers to pertinent literature on the subject (e.g., Jougnot et al., 2010; Revil,
 365 2013).

366 Finally, the relative electrokinetic coupling coefficient for partially saturated me-
 367 dia responds to

$$368 C_{EK}^{\text{rel}}(S_w, \omega) = \frac{C_{EK}(S_w, \omega)}{C_{EK}^0(S_w)}, \quad (28)$$

369 where $C_{EK}^0(S_w) = \lim_{\omega \rightarrow 0} C_{EK}(S_w, \omega)$.

370 Equations (24) and (26) are the central methodological result of this paper, as they
 371 define the saturation- and frequency-dependent effective excess charge density and elec-
 372 trokinetic coupling coefficient at the REV scale by means of a flux-averaging upscaling
 373 procedure. We remark that both $\hat{Q}_\nu^{\text{REV}}(S_w, \omega)$ and $C_{EK}(S_w, \omega)$ depend on the PSD of
 374 the probed medium, a characteristic that is included in the corresponding expressions
 375 via the $f(R)$ function.

3 Results

In this section, we analyze the effects of frequency and saturation on the effective excess charge density $\hat{Q}_v^{\text{REV}}(S_w, \omega)$ and the electrokinetic coupling coefficient $C_{EK}(S_w, \omega)$ in porous media. We assess the effects of the pore size distribution in the corresponding response by considering: (i) fractal, (ii) lognormal, and (iii) double-lognormal pore size distributions.

3.1 Pore Size Distribution

3.1.1 Fractal Distribution Function

As a first case, we consider a cumulative size distribution of pores whose radii are greater than or equal to R that obeys the following fractal law (e.g., Guarracino et al., 2014; Tyler & Wheatcraft, 1990; Yu et al., 2003)

$$N(R) = \left(\frac{R_{\max}}{R} \right)^D, \quad (29)$$

where D is the fractal dimension of the pore size with $1 < D < 2$ and $R_{\min} < R < R_{\max}$. The total number of pores, from R_{\min} to R_{\max} , is given by

$$N_t(R_{\min}) = \left(\frac{R_{\max}}{R_{\min}} \right)^D. \quad (30)$$

On the other hand, differentiating $N(R)$ with respect to R , we obtain the number of pores whose radii are between R and $R + dR$:

$$-dN = DR_{\max}^D R^{-D-1} dR = f(R) dR. \quad (31)$$

Dividing equations (31) and (30), we obtain the probability density function $f_r(R)$

$$-\frac{dN}{N_t} = DR_{\min}^D R^{-D-1} dR = f_r(R) dR, \quad (32)$$

such that,

$$\int_{R_{\min}}^{R_{\max}} f_r(R) dR = 1 - \left(\frac{R_{\min}}{R_{\max}} \right)^D \equiv 1, \quad (33)$$

which clearly holds if $(R_{\min}/R_{\max})^D \simeq 0$. In this sense, the condition $R_{\max} \gg R_{\min}$ must be satisfied for fractal analysis of porous media. Please note that, $f(R) = N_t f_r(R)$.

3.1.2 Lognormal Distribution Function

The lognormal distribution probability density function responds to

$$f_r(R) = \frac{1}{sR\sqrt{2\pi}} \exp\left(-\frac{(\log R - \mu)^2}{2s^2}\right). \quad (34)$$

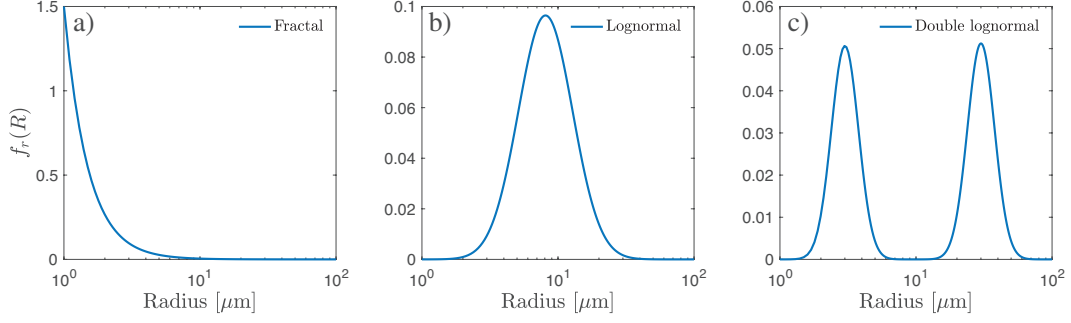


Figure 1. Probability density functions associated with the pore size distributions used in this work: (a) fractal ($D = 1.5$), (b) lognormal ($R^* = 10 \mu\text{m}$ and $\mathfrak{s} = 0.46$), and (c) double lognormal ($R_1^* = 3.1 \mu\text{m}$, $R_2^* = 31 \mu\text{m}$, $\mathfrak{s}_d = \mathfrak{s}/2$, $\beta_1 = 0.09$, and $\beta_2 = 0.91$).

403 where $\mathfrak{r} = \log R^*$ and \mathfrak{s} denote the scale and shape parameters. Again, we consider that
 404 $\mathfrak{f}(R) = N_t f_r(R)$, where N_t is the total number of pores in the medium.

405 **3.1.3 Double Lognormal Distribution Function**

406 The double lognormal distribution can be regarded as the sum of two lognormal
 407 distributions with the same shape parameter \mathfrak{s}_d and responds to

$$408 \quad f_r(R) = \beta_1 \frac{1}{\mathfrak{s}_d R \sqrt{2\pi}} \exp\left(-\frac{(\log R - \mathfrak{r}_1)^2}{2\mathfrak{s}_d^2}\right) + \beta_2 \frac{1}{\mathfrak{s}_d R \sqrt{2\pi}} \exp\left(-\frac{(\log R - \mathfrak{r}_2)^2}{2\mathfrak{s}_d^2}\right), \quad (35)$$

409 where $\mathfrak{r}_1 = \log R_1^*$ and $\mathfrak{r}_2 = \log R_2^*$, and $\beta_1 + \beta_2 = 1$. Again, we consider that $\mathfrak{f}(R) =$
 410 $N_t f_r(R)$.

411 Figure 1 shows the representative PSDs considered in this work with pore radius
 412 ranging from $1 \mu\text{m}$ to $100 \mu\text{m}$: (a) fractal ($D = 1.5$), (b) lognormal ($R^* = 10 \mu\text{m}$ and
 413 $\mathfrak{s} = 0.46$), and (c) double lognormal ($R_1^* = 3.1 \mu\text{m}$, $R_2^* = 31 \mu\text{m}$, $\mathfrak{s}_d = \mathfrak{s}/2$, $\beta_1 = 0.09$,
 414 and $\beta_2 = 0.91$). We remark that smaller pore radii dominate the response of the medium
 415 for fractal PSD, while pores distribute more evenly throughout the given radii for the
 416 lognormal and double lognormal PSDs. As shown below, the PSD characteristics result
 417 in significantly different responses for the effective permeability, the effective excess charge
 418 density, and, consequently, the electrokinetic coupling in porous media.

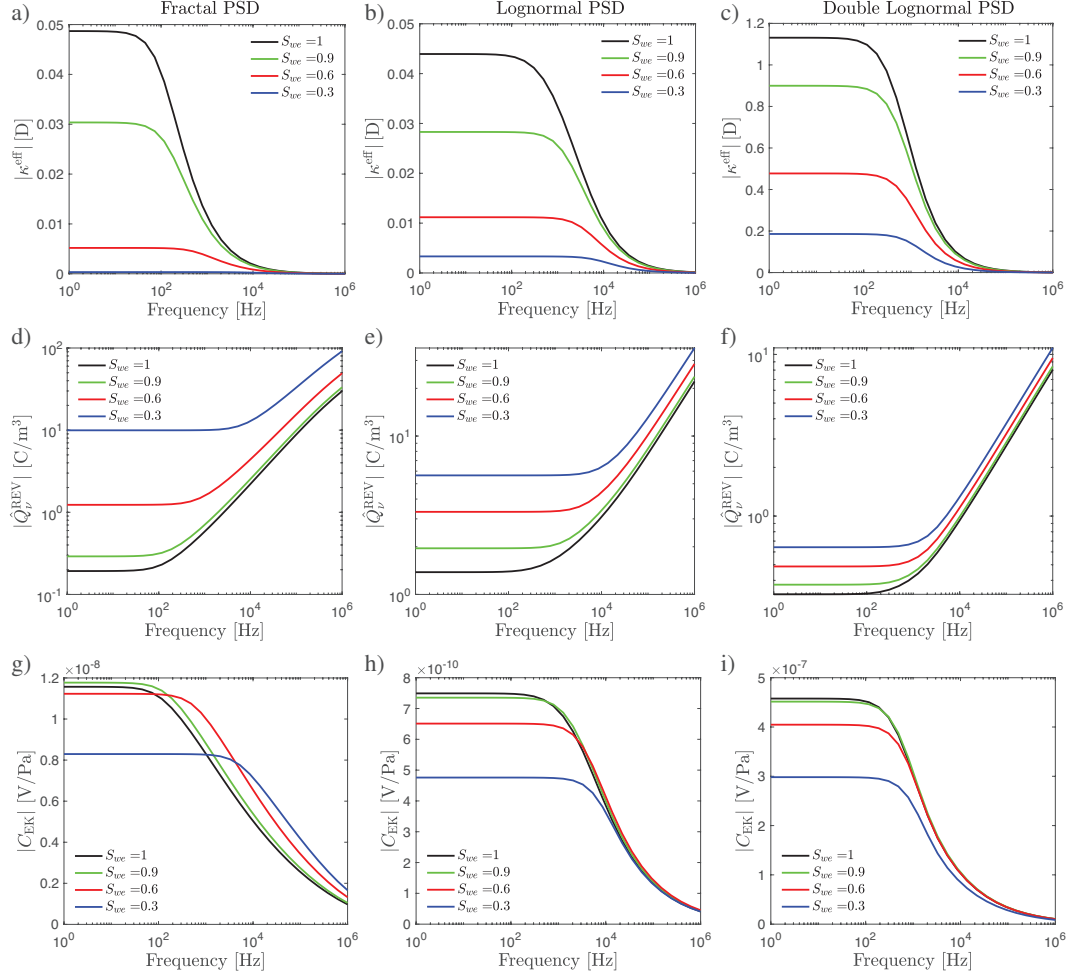


Figure 2. Absolute value of the effective dynamic permeability κ_w^{eff} , effective excess charge density \hat{Q}_ν^{REV} , and effective electrokinetic coupling coefficient C_{EK} as functions of frequency for different saturation states. Each row illustrates the result for a different PSD: (a, d, g) fractal ($D = 1.5$), (b, e, h) lognormal ($R^* = 10 \mu\text{m}$ and $\varepsilon = 0.46$), and (c, f, i) double lognormal ($R_1^* = 3.1 \mu\text{m}$, $R_2^* = 31 \mu\text{m}$, $\varepsilon_d = \varepsilon/2$, $\beta_1 = 0.09$, and $\beta_2 = 0.91$).

3.2 Numerical Analysis of the Proposed Model

Let us consider three porous media represented by: (i) a fractal PSD with a dimension $D = 1.5$, (ii) a lognormal PSD characterized by $R^* = 10 \mu\text{m}$ and $\mathfrak{s} = 0.46$, and (iii) a double lognormal PSD characterized by $R_1^* = 3.1 \mu\text{m}$, $R_2^* = 31 \mu\text{m}$, $\mathfrak{s}_d = \mathfrak{s}/2$, $\beta_1 = 0.09$, and $\beta_2 = 0.91$. We assume that they all have $\tau \simeq 1$, $R_{\min} = 1 \mu\text{m}$, and $R_{\max} = 100 \mu\text{m}$ and, also, the same total number of pores N_t , which is taken from the fractal distribution characteristics (equation 30). The pore fluid properties that saturate these probed media are summarized in Table 1.

Following Solazzi et al. (2020), we numerically solve equation (22) and obtain the saturation- and frequency-dependent effective permeability for the above described porous media. Figures 2a, 2b, and 2c illustrate the magnitude of $\kappa^{\text{eff}}(S_w, \omega)$ as a function of frequency for the three PSDs described above. Note that each column of Figure 2 is associated with one particular PSD. In this context, we plot different effective saturation states, identified by different colored lines. We observe that the absolute value of κ^{eff} decreases with frequency for $f > f_c$, with $f_c = \omega_c/2\pi$ denoting the critical frequency (Figures 2a, 2b, and 2c). Recall that f_c is determined by the PSD characteristics, specifically by the largest saturated pores of the distribution. The frequency-dependent behavior of $|\kappa^{\text{eff}}(S_w, \omega)|$ is explained by the onset of the inertia effects for $f \geq f_c$. When inertia effects prevail, the amplitude of the dynamic permeability drops and its phase increases (e.g., Zhou & Sheng, 1989). As previously observed by Solazzi et al. (2020), the critical frequency f_c increases with decreasing saturation, as water retreats to increasingly smaller pores. We also note that $|\kappa^{\text{eff}}|$ increases with water saturation. The corresponding response is modulated by the PSD of the probed porous medium. The reason behind this behavior is that the overall number of pores saturated by water decreases with decreasing S_w , as is the case in the classic relative permeability functions (e.g., Brooks & Corey, 1964; Mualem, 1976). Evidently, this saturation- and frequency-dependent behavior also affects \hat{Q}_ν^{REV} and C_{EK} at the REV scale. Note that, as expressed in equation (26), $C_{EK}(S_w, \omega)$ depends on $\kappa^{\text{eff}}(S_w, \omega)$ (equation 22), which includes both the effects of $\kappa(\omega)$ (equation 5) and $\kappa^{\text{rel}}(S_w, \omega)$ (equation 19).

Figures 2d, 2e, and 2f, illustrate the frequency dependence of the absolute value of the effective excess charge density $|\hat{Q}_\nu^{\text{REV}}(S_w, \omega)|$ at different effective saturation states (equation 24). The parameters of the PSDs and the physical properties of the wetting

Table 1. Fluid properties employed in this study.

| Definition | Variable | Value | Units |
|---------------------------------------|--------------|-------------------------|-------------------|
| Fluid shear viscosity (wetting phase) | η_w | 1×10^{-3} | Pa.s |
| Fluid density (wetting phase) | ρ_w | 1000 | kg/m ³ |
| Interfacial tension (water-air) | γ | 72×10^{-3} | N/m |
| Contact angle | β | 0 | rad |
| Dielectric permittivity of vacuum | ϵ_0 | 8.854×10^{-12} | F/m |
| Relative permittivity of the fluid | ϵ_r | 80.1 | - |
| Boltzmann constant | k_B | 1.381×10^{-23} | J/K |
| Avogadro number | N_A | 6.022×10^{23} | 1/Mol |
| Elementary charge | e_0 | 1.6×10^{-19} | C |
| Ionic concentration | C_{NaCl}^w | 10^{-4} | Mol/L |
| Temperature | T | 293.15 | K |

451 fluid are the same as those employed in panels 2a-2c of the corresponding figure. We ob-
 452 serve that $|\hat{Q}_\nu^{\text{REV}}(S_w, \omega)|$ increases with f for $f > f_c$ irrespective of the saturation. (Jougnot
 453 & Solazzi, 2021) explored the behavior of $\hat{Q}_\nu(\omega)$ in fully saturated conditions, and ob-
 454 served a corresponding increase for $f > f_c$. By comparing panels 2a to 2c with pan-
 455 els 2d to 2f, we observe identical shifts in the characteristic frequency $f_c(S_w)$, which moves
 456 towards higher frequencies for decreasing saturation. Again, this f_c -shift is different for
 457 each PSD, evidencing larger change of f_c with saturation for the fractal PSD than for
 458 the double lognormal PSD. Note that, as shown in previous works in fully saturated me-
 459 dia (e.g., Jougnot & Solazzi, 2021; Guarracino & Jougnot, 2018; Soldi et al., 2019), the
 460 magnitude of the effective excess charge density increases when the characteristic cap-
 461 illary size decreases. Consequently, the magnitude of $\hat{Q}_\nu^{\text{REV}}(S_w, \omega)$ increases with decreas-
 462 ing S_w , as water retreats towards relatively small pores. Both the fractal and the log-
 463 normal distribution characteristics, as considered in this section, present a larger num-
 464 ber of small pores when compared with the double lognormal PSD. This is precisely the
 465 reason for a larger relative variation in $\hat{Q}_\nu^{\text{REV}}(S_w, \omega)$ values for the fractal and lognor-
 466 mal PSDs for decreasing saturations as compared with those associated with the dou-
 467 ble lognormal PSD.

468 Finally, using equations (21) to (27), we predict the frequency dependence of the
 469 electrokinetic coupling coefficient C_{EK} at different saturation states (Figs 2g, 2h, and
 470 2i). We consider the previously described PSDs and pore fluid properties, together with
 471 representative values of $\sigma_s = 3 \times 10^{-3}$ S/m, $S_{wr} = 0.2$, $n = 1.7$ and $F = 5$ to model
 472 the variation of electrical conductivity of porous media as a function of water saturation
 473 S_w . To infer the electrical conductivity σ_w from C^w , we employ the relation $\sigma_w = 10 \times$
 474 C^w for a NaCl solution (Sen & Goode, 1992). The results show that the magnitude of
 475 C_{EK} decreases with increasing frequency for $f > f_c$ irrespective of S_w (Figs 2g, 2h, and
 476 2i). This behavior is in good match with published works for the case of full saturation
 477 (e.g., Jougnot & Solazzi, 2021; Pride, 1994; Revil & Mahardika, 2013). Even though the
 478 amplitude of C_{EK} appears to decrease with decreasing S_w for lognormal (Fig. 2h) and
 479 double lognormal PSDs (Fig. 2i), this is not the case for the fractal PSD (Fig. 2g). In
 480 the latter case, we note that the amplitude of C_{EK} increases and, then, decreases with
 481 saturation, a behavior that is more clearly illustrated below (Figure 3).

482 For completeness, we illustrate the behavior of κ_w^{eff} , \hat{Q}_ν^{REV} , and C_{EK} as functions
 483 of the effective saturation S_{we} , for different frequencies (Figure 3). Black circled lines
 484 denote the so-called low frequency limit for κ_w^{eff} , \hat{Q}_ν^{REV} , and C_{EK} , while colored lines de-
 485 pict the responses for $f = 10^2$ Hz, $f = 10^3$ Hz, and $f = 10^4$ Hz. We observe that all
 486 curves tend to the same value for sufficiently small S_{we} values, irrespective of the prob-
 487 ing frequency. This is expected, as f_c shifts towards higher frequencies for decreasing sat-
 488 urations (see Figure 2). Hence, the probing frequencies became smaller than f_c for suf-
 489 ficiently low saturations and κ_w^{eff} , \hat{Q}_ν^{REV} , and C_{EK} tend to their low-frequency counter-
 490 parts. Conversely, for increasing S_{we} , the overall responses experience a departure from
 491 the low-frequency behavior. Figure 3 evidences the control that the PSD has on $\kappa_w^{\text{eff}}(S_w)$,
 492 $\hat{Q}_\nu^{\text{REV}}(S_w)$, and $C_{EK}(S_w)$ for different probing frequencies, as we note different slopes
 493 and inflections for different PSDs.

494 4 Discussion

495 In this section, we compare the $\hat{Q}_\nu^{\text{REV}}(\omega, S_w)$ estimates obtained by means of the
 496 proposed flux-averaging approach with respect to those predicted by the pioneering model
 497 of Revil and Mahardika (2013). Then, we address the capability of the proposed model
 498 to predict experimental measurements of $C_{EK}^{\text{rel}}(\omega, S_w)$ which, to date, have been only per-
 499 formed under fully saturated conditions ($S_w = 1$).

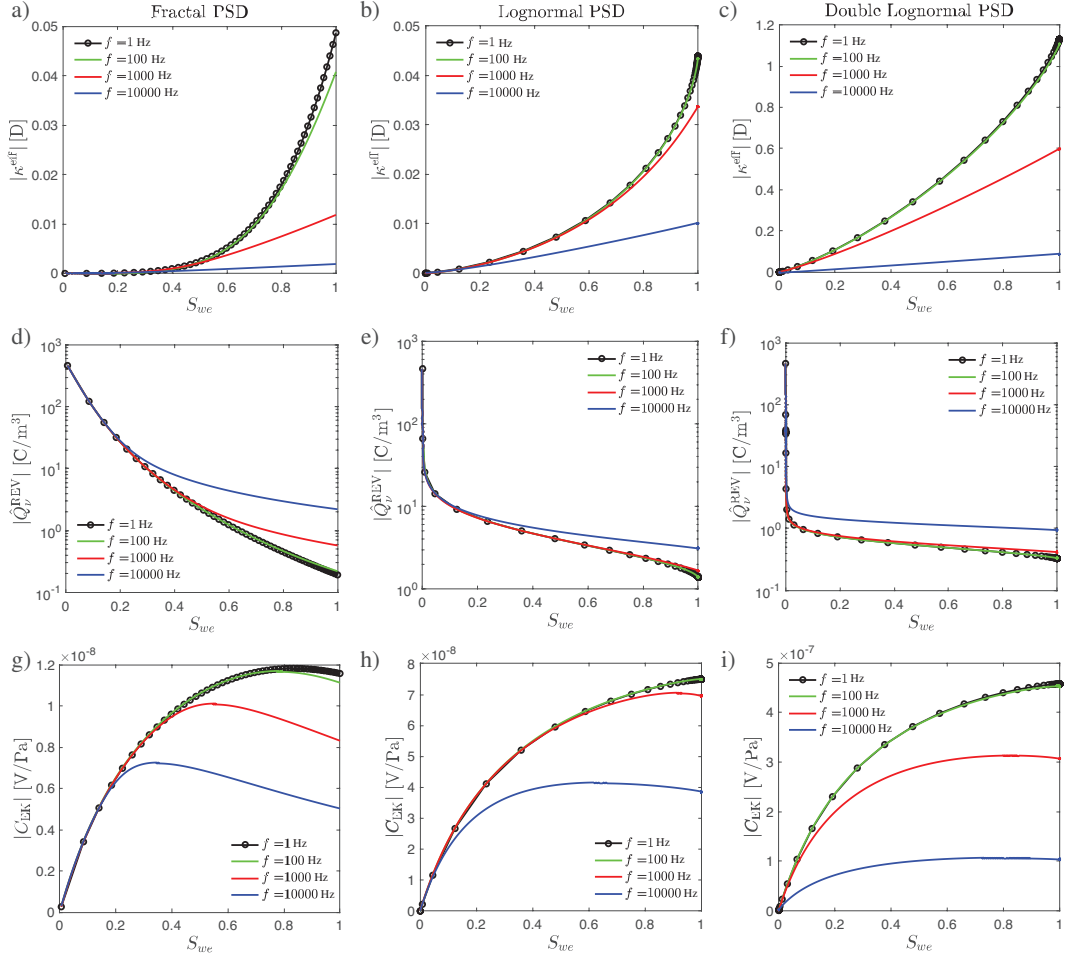


Figure 3. Absolute value of the effective dynamic permeability κ_w^{eff} , effective excess charge density \hat{Q}_ν^{REV} , and effective electrokinetic coupling coefficient C_{EK} as functions of saturation for different frequencies. Each row illustrates the result for a different PSD: (a, d, g) fractal ($D = 1.5$); (b, e, h) lognormal ($R^* = 10 \mu\text{m}$ and $\varsigma = 0.46$); and (c, f, i) double lognormal ($R_1^* = 3.1 \mu\text{m}$, $R_2^* = 31 \mu\text{m}$, $\varsigma_d = \varsigma/2$, $\beta_1 = 0.09$, and $\beta_2 = 0.91$).

500 **4.1 Comparison with Previous Models**

501 In their classical work, Revil and Mahardika (2013) proposed the following empir-
502 ical model for the frequency- and saturation-dependent effective excess charge density

503
$$\hat{Q}_\nu^{\text{REV}}(S_w, \omega) \simeq \hat{Q}_\nu^0(S_w) \sqrt{1 - i\omega\tau_k(S_w)}, \quad (36)$$

504 where $\hat{Q}_\nu^0(S_w)$ denotes the low-frequency value of the effective excess charge density and
505 τ_k denotes the relaxation time of the frequency-dependent behavior, which is given by

506
$$\tau_k(S_w) = \kappa^{\text{eff}}(S_w) \frac{\rho_w F S_w^{1-n}}{\eta_w}. \quad (37)$$

507 In order to compute equation (36), Revil and Mahardika (2013) use the volume
508 averaging model of Linde et al. (2007)

509
$$\hat{Q}_\nu^0(S_w) \simeq \frac{\hat{Q}_\nu^{\text{sat},0}}{S_w}. \quad (38)$$

510 where $\hat{Q}_\nu^{\text{sat},0}$ is the low-frequency effective excess charge density in fully saturated con-
511 ditions. To estimate $\kappa^{\text{eff}}(S_w)$, the authors take the Brooks and Corey (1964) model

512
$$\kappa^{\text{eff}}(S_w) = \kappa_0 S_w^{\frac{2+3\lambda}{\lambda}}, \quad (39)$$

513 with λ a fitting parameter that is determined by the pore space characteristics of the probed
514 medium.

515 It is important to remark that equation (36) is based on a linear and low-frequency
516 approximation of the dynamic permeability, which is commonly used to deal with $\kappa(\omega)$
517 in the space-time domain (e.g., Revil & Mahardika, 2013). Given that the proposed flux-
518 averaging approach (equation 24) is developed in the space-frequency domain, our es-
519 timates are not limited by such assumption. More importantly, in equation (36), Revil
520 and Mahardika (2013) assume that equations (38) and (39) hold for the probed medium.
521 If we wish to compare our approach with such model, it is important to analyze first the
522 validity of equations (38) and (39) for the considered PSDs.

523 Figure 4 shows a comparison between equations (38) and (39) with the correspond-
524 ing ones considered in this work, which respond to equations (6) and (24) (in the low
525 frequency). We observe that equation (39) correctly reproduces the tendencies of the ef-
526 fective permeability associated with the fractal PSD (Figure 4a), which is in agreement
527 with the observations of Soldi et al. (2017) for fractal media. Considering typical λ val-
528 ues, we note that equation (39) tends to underestimate $\kappa^{\text{eff},0}(S_w)$ for lognormal and dou-
529 ble lognormal PSDs (Figures 4b and 4c). We remark that the considered pore-structure

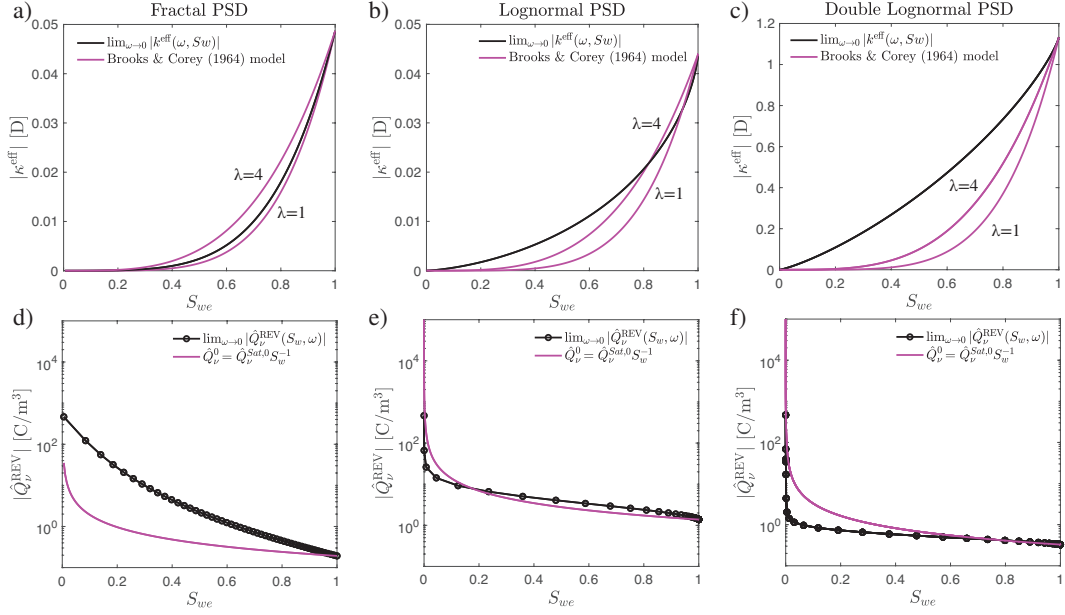


Figure 4. (a, b, c) Effective permeability and effective excess charge density as a function of the effective saturation in the low-frequency limit for: (a, d) fractal ($D = 1.8$, $R_{\min} = 23$ nm and $R_{\max} = 4.7$ μm), (b, e) lognormal ($R^* = 1.4$ μm and $\mathfrak{s} = 0.15$), and (c, d) double lognormal ($R_1^* = 1.0$ μm , $R_2^* = 1.5$ μm , $\mathfrak{s}_d = \mathfrak{s}/2$, $\beta_1 = 0.4$, and $\beta_2 = 0.6$) PSDs. Panels (a, b, c) illustrate the behavior of equation (39) for $\lambda = \{1, 4\}$ (magenta solid lines) and that of equation (6) (black circled lines). Panels (d, e, c) illustrate the behavior predicted by equation (38) (magenta solid lines) compared with that of (24) in the low-frequency range (black circled lines).

530 is highly idealized and these differences can be a source of mismatch, as equation (39)
 531 is known to provide reliable predictions of $\kappa^{\text{eff},0}(S_w)$ in siliciclastic rocks. On the other
 532 hand, Figures 4d to 4f allow us to test the assumption expressed in equation (38). In-
 533 terestingly, we note that this equation provides with a fair representation of $\lim_{\omega \rightarrow 0} |\hat{Q}_\nu^{\text{REV}}|$
 534 when considering a lognormal PSD. However, it tends to give biased representations of
 535 the corresponding variable for fractal and double lognormal PSDs. Particularly, equa-
 536 tion (38) results in estimations that significantly differ from those predicted by the low-
 537 frequency limit of equation (24) for low saturations. We conclude that, when compar-
 538 ing the proposed approach with that of Revil and Mahardika (2013) (equation 36), dif-
 539 ferences associated with the estimates given by equations (38) and (39) may be a source
 540 of mismatch. In order to circumvent this issue and, also, given that performing low-frequency
 541 measurements of $\kappa^{\text{eff},0}(S_w)$ and $\hat{Q}_\nu^{\text{REV},0}(S_w)$ is feasible in laboratory setups, in the fol-
 542 lowing, we propose to perform the comparison of equations (24) and (36) assuming that
 543 $\kappa^{\text{eff},0}(S_w)$ and $\hat{Q}_\nu^{\text{REV},0}(S_w)$ are known and, in this case, given by those resulting from
 544 the flux-averaging approach proposed in this work. As such, below, we concentrate solely
 545 on comparing the frequency-dependent response predicted by our model and that of Revil
 546 and Mahardika (2013).

547 Figure 5 shows a comparison between the results from equation (24) (solid lines)
 548 and (36) (dashed lines) for the proposed PSDs, at each column. The first row depicts
 549 the absolute value of $|\hat{Q}_\nu^{\text{REV}}(S_w, \omega)|$ as a function of frequency (for different saturation
 550 states) and the second row the corresponding behavior as a function of saturation (for
 551 different probing frequencies). We observe that, in general, the proposed flux-averaging
 552 model and the model of Revil and Mahardika (2013) provide with similar tendencies. In
 553 particular, estimates are largely similar for saturations approaching unity (Figures 5a
 554 to 5c) and at relatively low frequencies (Figures 5d to 5f). Given that the proposed model
 555 obtained the corresponding estimates, for the first time in the literature, averaging the
 556 physical processes from the pore to the REV scale, we are thus validating the model of
 557 Revil and Mahardika (2013) and proving its consistency and robustness despite its sim-
 558 plicity.

559 4.2 Comparison with Experimental Data

560 To date, measurements of $C_{EK}^{\text{rel}}(\omega)$ for different probing frequencies have been per-
 561 formed only under fully saturated conditions. The proposed model should have the ca-

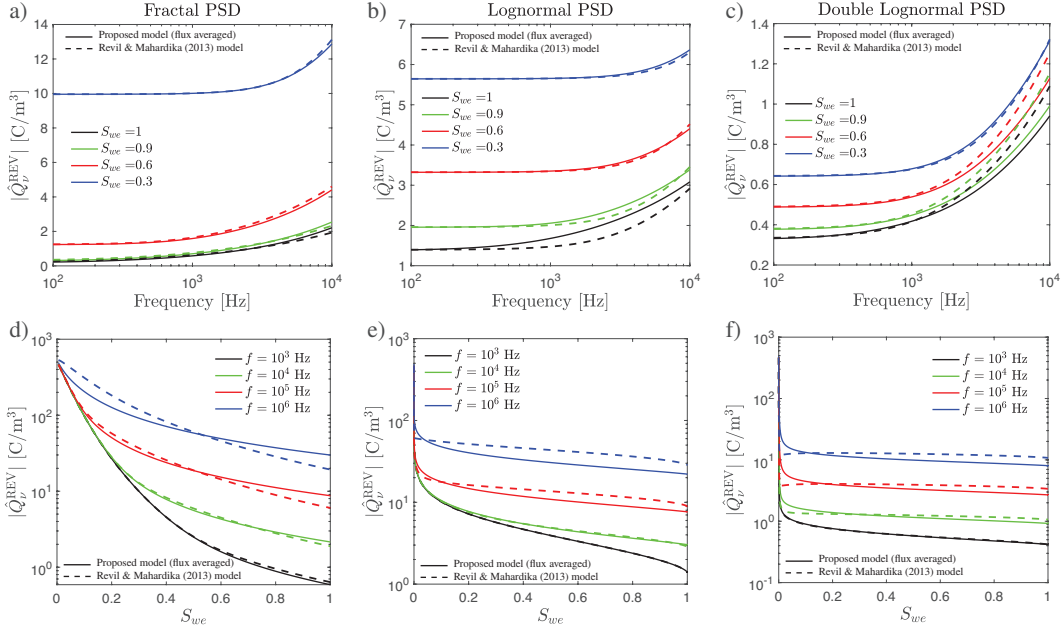


Figure 5. Effective excess charge density as a function of (a, b, c) frequency and (d, e, f) of the effective saturation. We consider: (a, d) a fractal PSD ($D = 1.8$, $R_{\min} = 23 \mu\text{m}$ and $R_{\max} = 4.7 \mu\text{m}$, $m = 1.19$); (b, e) a lognormal PSD ($R^* = 1.4 \mu\text{m}$ and $\mathfrak{s} = 0.15$, $m = 1.06$), and (c, f) a double lognormal PSD ($R_1^* = 1.0 \mu\text{m}$, $R_2^* = 1.5 \mu\text{m}$, $\mathfrak{s}_d = \mathfrak{s}/2$, $\beta_1 = 0.4$, and $\beta_2 = 0.6$, $m = 1$) PSDs. Solid lines illustrate the behavior of the proposed flux-averaging model (equation 24) and dashed lines illustrate the behavior predicted by Revil and Mahardika (2013) model (equation 36).

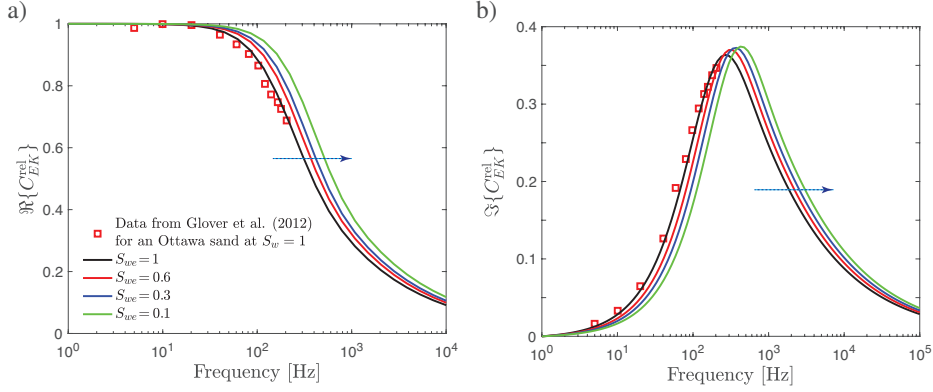


Figure 6. (a) Real and (b) imaginary parts of the relative electrokinetic coupling coefficient as functions of frequency. We illustrate results of the proposed model for different saturations (solid lines) using a lognormal PSD. Red squares depict the experimental measurements of Glover, Walker, and Jackson (2012) for an Ottawa sand at full saturation. We also illustrate the predictions of the proposed model for other saturations (colored lines). The dashed blue arrows indicate the direction in which saturation decreases.

562 pability of representing experimental measurements in such end-member scenario of sat-
 563 turation and, also, to predict the partially saturated response of the corresponding me-
 564 dia.

565 Figure 6 shows the frequency dependence of the real and imaginary parts of $C_{EK}^{rel}(\omega)$
 566 at fully saturated conditions as reported by Glover, Walker, Ruel, and Tardif (2012) for
 567 an Ottawa sand sample. The Ottawa sand is characterized by a mean grain radius of 235
 568 μm . Glover, Walker, Ruel, and Tardif (2012) used a 10^{-3} mol/L NaCl electrolyte. We
 569 employed a lognormal PSD in combination with equation (17), that is equation (28) with
 570 $S_w=1$, to model the behavior of the measured data. We take $R_{min} = 1.05 \mu\text{m}$ and $R_{min} =$
 571 $105 \mu\text{m}$, as well as $R^* = 60 \mu\text{m}$ and $s = 0.15$. Note that R^* is close to the effective pore
 572 radii of $r_p = 67 \mu\text{m}$, as reported by Glover, Walker, Ruel, and Tardif (2012) for the cor-
 573 responding sample. The pore fluid properties are summarized in Table 1. We observe
 574 that the proposed model is able to reproduce experimental data (Figure 6, black lines).
 575 We also illustrate variations predicted by the proposed model for C_{EK}^{rel} for saturations
 576 of $S_w = 0.6, 0.3$ and 0.1 (Figure 6, colored lines). The dashed blue arrows indicate the
 577 direction in which saturation decreases in Figures 6a and 6b, evidencing an increase of

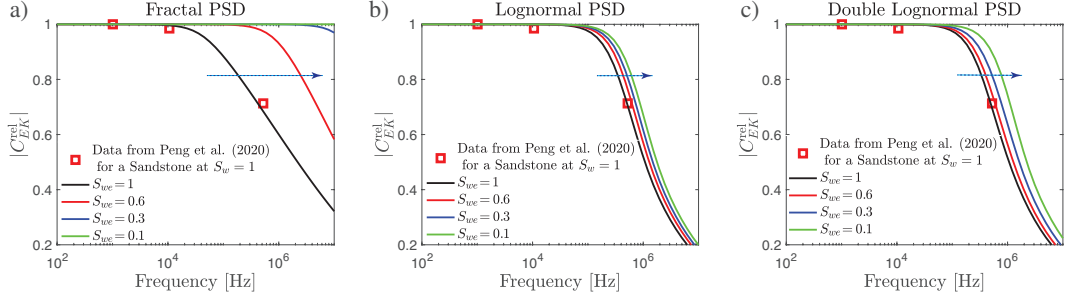


Figure 7. Amplitude of the electrokinetic coupling coefficient as function of frequency for different saturations. Each column displays the results for a different PSDs: (a) fractal ($D = 1.8$, $R_{\min} = 23$ nm and $R_{\max} = 4.7$ μm), (b) lognormal ($R^* = 1.4$ μm and $\varepsilon = 0.15$), and (c) double lognormal ($R_1^* = 1.0$ μm , $R_2^* = 1.5$ μm , $\varepsilon_d = \varepsilon/2$, $\beta_1 = 0.4$, and $\beta_2 = 0.6$). Red squares depict the experimental measurements of Peng et al. (2020) for a fully saturated sandstone. We also illustrate the predictions of the proposed model for other saturations (colored lines). The dotted blue arrows indicate the direction in which saturation decreases.

578 f_c with decreasing S_w , a fact that is also observed in the effective permeability curves
 579 for lognormal distributions (Figure 2b).

580 Figures 7 shows the frequency dependence of $|C_{EK}^{rel}|$ at full saturation for a sandstone
 581 sample, as measured by Peng et al. (2020) (red squares). We show that the proposed
 582 model is capable of fitting the main trend of experimental data by means of the
 583 three PSD described in this study, by using: (a) fractal ($D = 1.8$, $R_{\min} = 23$ nm and
 584 $R_{\max} = 4.7$ μm), (b) lognormal ($R^* = 1.4$ μm and $\varepsilon = 0.15$), and (c) double lognor-
 585 mal ($R_1^* = 1.0$ μm , $R_2^* = 1.5$ μm , $\varepsilon_d = \varepsilon/2$, $\beta_1 = 0.4$, and $\beta_2 = 0.6$). We remark that,
 586 because of computational restrictions involved with the numerical integrations performed
 587 in this work, we do not carry out a full inversion of the parameters but empirically find
 588 those which provide a relatively good fit with experimental data. Nevertheless, these pa-
 589 rameters are similar to those reported by Thanh et al. (2021) for the same sample to model
 590 the frequency dependence of the electrokinetic coupling coefficient, that is directly ex-
 591 pressed via the Zeta potential rather than the effective excess charge density. Once again,
 592 we illustrate the predicted variations of $|C_{EK}^{rel}|$ for different saturations (colored lines).

593 Finally, Figure 8 shows the frequency dependence of $|C_{EK}|$ measured by Zhu and
 594 Toksoz (2013) for a sample of Berea sandstone (squared curves) for different electrical
 595 conductivities. We employ the proposed model considering $R_{\min} = 0.13$ μm and $R_{\max} =$

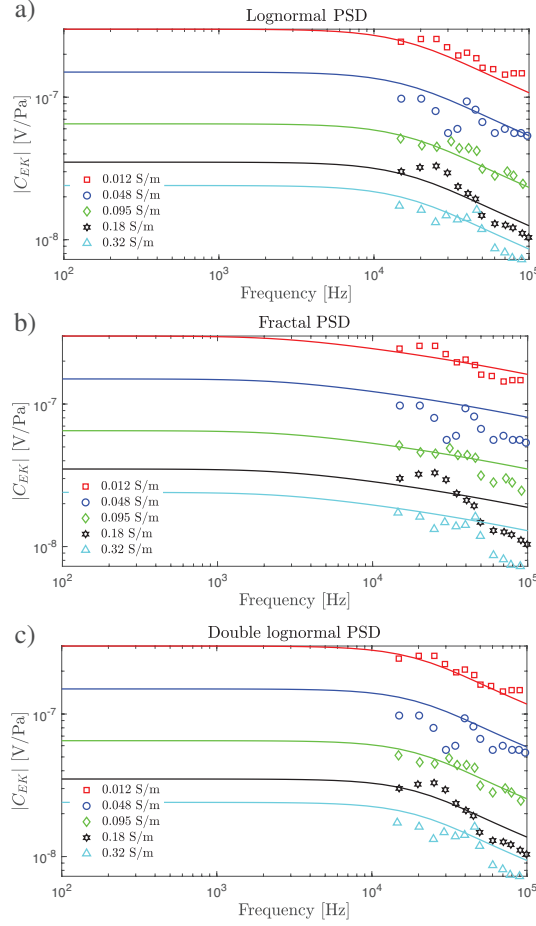


Figure 8. Amplitude of the electrokinetic coupling coefficient as functions of frequency under saturated conditions for different electrical conductivities. Colored squares denote measurements taken by Zhu and Toksoz (2013) for a Berea sandstone. We illustrate the predictions of the proposed model for three different PSDs: (a) fractal ($D = 1.65$, $R_{\min} = 0.13 \mu\text{m}$ and $R_{\max} = 30 \mu\text{m}$), (b) lognormal ($R^* = 6.3 \mu\text{m}$ and $\mathfrak{s} = 0.15$, $R_{\min} = 0.13 \mu\text{m}$ and $R_{\max} = 30 \mu\text{m}$), and (c) double lognormal ($R_1^* = 1.0 \mu\text{m}$, $R_2^* = 3.0 \mu\text{m}$, $\mathfrak{s}_d = \mathfrak{s}/2$, $\beta_1 = 0.4$, and $\beta_2 = 0.6$).

596 $30 \mu\text{m}$ for the different PSD (see solid lines), that is, (a) fractal ($D = 1.65$), (b) lognor-
 597 mal ($R^* = 6.3 \mu\text{m}$ and $\mathfrak{s} = 0.15$) and (c) double lognormal ($R_1^* = 1.0 \mu\text{m}$, $R_2^* = 3.0 \mu\text{m}$,
 598 $\mathfrak{s}_d = \mathfrak{s}/2$, $\beta_1 = 0.4$, and $\beta_2 = 0.6$). The values of C_{EK}^0 are reported to be 0.3×10^{-6} ,
 599 0.15×10^{-6} , 0.065×10^{-6} , 0.035×10^{-6} and 0.024×10^{-6} V/Pa for 0.012, 0.048, 0.095, 0.18
 600 and 0.32 S/m, respectively (Zhu & Toksoz, 2013). Using equation (17), we are able to
 601 obtain C_{EK}^{rel} and, hence, C_{EK} . It is seen that the proposed approach using three con-
 602 sidered PSDs is capable of reproducing the experimental data very well.

5 Conclusions

We proposed a flux averaging approach to compute the frequency- and saturation-dependent effective excess charge density in partially saturated porous media. For this, we conceptualized the pore space as a bundle of capillary tubes with a given pore size distribution (PSD). We modeled the frequency dependence of the effective excess charge density by solving the Navier-Stokes equations under oscillatory flow conditions within the capillaries that are effectively saturated for a given capillary pressure state. Overall, we derived expressions for: (i) the capillary pressure–saturation relationship of the probed medium; and for the saturation- and frequency-dependent (ii) effective permeability $\kappa^{\text{eff}}(S_w, \omega)$, (iii) effective excess charge density $\hat{Q}_\nu^{\text{REV}}(S_w, \omega)$, and (iv) electrokinetic coupling coefficient $C_{\text{EK}}(S_w, \omega)$.

The variation of κ^{eff} , \hat{Q}_ν^{REV} and C_{EK} with frequency at different saturation states are analyzed and explained for three different PSDs (fractal, lognormal and double lognormal PSDs). It is shown that the PSD has strong effect on the critical frequency ω_c and the characteristics of κ^{eff} , \hat{Q}_ν^{REV} and C_{EK} as functions of frequency and saturation. Namely, the critical frequency ω_c increases with decreasing water saturation S_w for a given PSD. The reason is that when the water saturation decreases, only the smaller radius pores are saturated by water, leading to a decrease of the characteristic radius representative \tilde{R} of the saturated pores. This process affects the effective excess charge density at the REV scale. The proposed model is compared with previous models in the literature and, in the case of full saturation, it is also compared with published data. We found that the proposed model is capable of reproducing the frequency-dependence of \hat{Q}_ν^{REV} as predicted by previous models, which do not rely in a flux-averaging approach, provided that the low-frequency estimates of the effective excess charge and effective permeability are correct. On the other hand, our approach was able to represent experimental measurements of the coupling coefficient C_{EK} for different frequencies, conductivities, and rock properties. The proposed approach is valid for practically any PSD and constitutes a practical framework for the interpretation of seismoelectric signatures of partially saturated media.

Data Availability Statement

The data and computational codes associated with this paper are available online from <https://doi.org/10.5281/zenodo.6620462>.

Acknowledgments

L. D. T thanks the Vietnam National Foundation for Science and Technology Development (NAFOSTED), grant number 103.99-2019.316. D. J. acknowledge the support of the GeoProcesS project funded by the Emergence(s) Ville de Paris program. K. H. thanks the support from the National Natural Science Foundation of China under Grant 42104069.

References

- Auriault, J.-L., Borne, L., & Chambon, R. (1985). Dynamics of porous saturated media, checking of the generalized law of Darcy. *J. Acoust. Soc. Am.*, *77*(5), 1641–1650.
- Bear, J. (1972). *Dynamics of Fluids in Porous Media*. N. Y.: Elsevier.
- Blunt, M. J. (2017). *Multiphase Flow in Permeable Media: A Pore-Scale Perspective*. Cambridge University Press.
- Bordes, C., Sénéchal, P., Barrière, J., Brito, D., Normandin, E., & Jougnot, D. (2015). Impact of water saturation on seismoelectric transfer functions: a laboratory study of coseismic phenomenon. *Geophys. J. Int.*, *200*(3), 1317-1335.
- Brooks, R., & Corey, A. (1964). *Hydraulic properties of porous media*. Colorado State University.
- Butler, K. E. (1996). *Seismoelectric effects of electrokinetic origin*. PhD thesis, University of British Columbia.
- Collini, H., & Jackson, M. D. (2022). Relationship between zeta potential and wettability in porous media: insights from a simple bundle of capillary tubes model. *J. Colloid Interface Sci.*, *608*, 605–621.
- Dupuis, J. C., Butler, K. E., & Kepic, A. W. (2007). Seismoelectric imaging of the vadose zone of a sand aquifer. *Geophysics*, *72*(6), A81–A85.
- Gao, Y., Harris, J. M., Wen, J., Huang, Y., Twardzik, C., Chen, X., & Hu, H. (2016). Modeling of the coseismic electromagnetic fields observed during the 2004 Mw 6.0 Parkfield earthquake. *Geophys. Res. Lett.*, *43*(2), 620–627.
- Garambois, S., & Dietrich, M. (2001). Seismoelectric wave conversions in porous

- 663 media: Field measurements and transfer function analysis. *Geophysics*, 66(5),
664 1417–1430.
- 665 Glover, P. W. J., Walker, E., & Jackson, M. (2012). Streaming-potential coefficient
666 of reservoir rock: A theoretical model. *Geophysics*, 77(2)(2), D17-D43.
- 667 Glover, P. W. J., Walker, E., Ruel, J., & Tardif, E. (2012). Frequency-dependent
668 streaming potential of porous media-part 2: Experimental measurement of
669 unconsolidated materials. *Int. J. Geophys.*, 2012.
- 670 Grobbe, N., Revil, A., Zhu, Z., & Slob, E. (2020). *Seismoelectric exploration: The-*
671 *ory, experiments, and applications* (Vol. 252). John Wiley & Sons.
- 672 Guarracino, L., & Jougnot, D. (2018). A physically based analytical model to
673 describe effective excess charge for streaming potential generation in water
674 saturated porous media. *J. Geophys. Res.: Solid Earth*, 123(1), 52-65.
- 675 Guarracino, L., Rötting, T., & Carrera, J. (2014). A fractal model to describe the
676 evolution of multiphase flow properties during mineral dissolution. *Adv Water*
677 *Resour*, 67, 78–86.
- 678 Han, S.-J., Kim, S.-S., & Kim, B.-I. (2004). Electroosmosis and pore pressure
679 development characteristics in lead contaminated soil during electrokinetic
680 remediation. *Geosci. J.*, 8(1), 85–93.
- 681 Jaafar, M. Z., Vinogradov, J., & Jackson, M. D. (2009). Measurement of streaming
682 potential coupling coefficient in sandstones saturated with high salinity nacl
683 brine. *Geophys. Res. Lett.*, 36(L21306), doi:10.1029/2009GL040549.
- 684 Jackson, M. D. (2010). Multiphase electrokinetic coupling: Insights into the impact
685 of fluid and charge distribution at the pore scale from a bundle of capillary
686 tubes model. *J. Geophys. Res.: Solid Earth*, 115(B7).
- 687 Johnson, D. L., Koplik, J., & Dashen, R. (1987). Theory of dynamic permeability
688 and tortuosity in fluid-saturated porous media. *J. Fluid Mech.*, 176, 379-402.
689 doi: 10.1017/S0022112087000727
- 690 Jougnot, D., Linde, N., Revil, A., & Doussan, C. (2012). Derivation of soil-specific
691 streaming potential electrical parameters from hydrodynamic characteristics of
692 partially saturated soils. *Vadose Zone J.*, 11(1), 272-286.
- 693 Jougnot, D., Mendieta, A., Leroy, P., & Maineult, A. (2019). Exploring the effect
694 of the pore size distribution on the streaming potential generation in saturated
695 porous media, insight from pore network simulations. *J. Geophys. Res.: Solid*

- 696 *Earth*, 124(6), 5315–5335.
- 697 Jougnot, D., Revil, A., Ghorbani, A., Leroy, P., & Cosenza, P. (2010). Spectral
698 induced polarization of partially saturated clay-rocks: a mechanistic approach.
699 *Geophys. J. Int.*, 180(1), 210–224.
- 700 Jougnot, D., Roubinet, D., Guarracino, L., & Maineult, A. (2020). Modeling stream-
701 ing potential in porous and fractured media, description and benefits of the
702 effective excess charge density approach. In *Advances in Modeling and Inter-
703 pretation in Near Surface Geophysics* (pp. 61–96). Springer.
- 704 Jougnot, D., Rubino, J. G., Carbajal, M. R., Linde, N., & Holliger, K. (2013).
705 Seismoelectric effects due to mesoscopic heterogeneities. *Geophys. Res. Lett.*,
706 40(10), 2033–2037.
- 707 Jougnot, D., & Solazzi, S. G. (2021). Predicting the frequency-dependent effective
708 excess charge density: A new up-scaling approach for seismoelectric modelling.
709 *Geophysics*, 86(3), 1–10.
- 710 Kozeny, J. (1927). Über kapillare Leitung des Wassers im Boden. *Akad. Wiss.*,
711 136(2a), 271–306.
- 712 Li, J. X., Rezaee, R., & Müller, T. M. (2020). Wettability effect on wave propaga-
713 tion in saturated porous medium. *J. Acoust. Soc.*, 147(2), 911–920.
- 714 Li, J. X., Rezaee, R., Müller, T. M., & Sarmadivaleh, M. (2021). Pore size
715 distribution controls dynamic permeability. *Geophys. Res. Lett.*, 48(5),
716 e2020GL090558.
- 717 Linde, N., Jougnot, D., Revil, A., Matthäi, S., Arora, T., Renard, D., & Doussan, C.
718 (2007). Streaming current generation in two-phase flow conditions. *Geophys.
719 Res. Lett.*, 34(3).
- 720 Mavko, G., Mukerji, T., & Dvorkin, J. (2009). *The rock physics handbook: Tools for
721 seismic analysis of porous media*. Cambridge University Press.
- 722 Monachesi, L. B., Zyserman, F. I., & Jouniaux, L. (2018). An analytical solution
723 to assess the sh seismoelectric response of the vadose zone. *Geophys. J. Int.*,
724 213(3), 1999–2019.
- 725 Mualem, Y. (1976). A new model for predicting the hydraulic conductivity of unsat-
726 urated porous media. *Water Resour. Res.*, 12(3), 513–522.
- 727 Packard, R. G. (1953). Streaming potentials across glass capillaries for sinusoidal
728 pressure. *J. Chem. Phys.*, 21(2), 303–307.

- 729 Peng, R., Di, B., Glover, P. W. J., Wei, J., Lorinczi, P., Liu, Z., & Li, H. (2020).
730 Seismo-electric conversion in shale: experiment and analytical modelling. *Geo-*
731 *phys. J. Int.*, *223*(2), 725-745.
- 732 Pride, S. R. (1994). Governing equations for the coupled electromagnetics and
733 acoustics of porous media. *Phys. Rev. B*, *50*(21), 15678.
- 734 Pride, S. R., & Morgan, F. D. (1991). Electrokinetic dissipation induced by seismic
735 waves. *Geophysics*, *56*(7), 914-925.
- 736 Reppert, P. M. (2001). Frequency-dependent streaming potentials. *J. Colloid and*
737 *Interf. Sci.*, *234*(1), 194 - 203. doi: 10.1006/jcis.2000.7294
- 738 Revil, A. (2013). Effective conductivity and permittivity of unsaturated porous ma-
739 terials in the frequency range 1 mHz–1GHz. *Water Resour. Res.*, *49*(1), 306-
740 327.
- 741 Revil, A., & Jardani, A. (2010). Seismoelectric response of heavy oil reservoirs: the-
742 ory and numerical modelling. *Geophys. J. Int.*, *180*(2), 781–797.
- 743 Revil, A., Jardani, A., Sava, P., & Haas, A. (2015). *The seismoelectric method: The-*
744 *ory and applications*. John Wiley & Sons.
- 745 Revil, A., & Mahardika, H. (2013). Coupled hydromechanical and electromag-
746 netic disturbances in unsaturated porous materials. *Water Resour. Res.*, *49*,
747 744-766.
- 748 Rosas-Carbaljal, M., Jougnot, D., Rubino, J. G., Monachesi, L., Linde, N., & Hol-
749 liger, K. (2020). Seismoelectric signals produced by mesoscopic heterogeneities:
750 Spectroscopic analysis of fractured media. *Seismoelectric Exploration: Theory,*
751 *Experiments, and Applications*, 269–287.
- 752 Sen, P. N., & Goode, P. A. (1992). Influence of temperature on electrical conductiv-
753 ity on shaly sands. *Geophysics*, *57*(1), 89-96.
- 754 Smeulders, D., Eggels, R., & Van Dongen, M. (1992). Dynamic permeability: refor-
755 mulation of theory and new experimental and numerical data. *J. Fluid Mech.*,
756 *245*, 211–227.
- 757 Solazzi, S. G., Rubino, J. G., Jougnot, D., & Holliger, K. (2020). Dynamic perme-
758 ability functions for partially saturated porous media. *Geophys. J. Int.*, *221*(2),
759 1182–1189.
- 760 Soldi, M., Guarracino, L., & Jougnot, D. (2017). A simple hysteretic constitutive
761 model for unsaturated flow. *Transport Porous Med.*, *120*(2), 271–285.

- 762 Soldi, M., Guarracino, L., & Jougnot, D. (2019). An analytical effective excess
763 charge density model to predict the streaming potential generated by unsatu-
764 rated flow. *Geophys. J. Int.*, *216*(1), 380-394.
- 765 Thanh, L. D., Jougnot, D., Solazzi, S. G., Van Nghia, N., & Van Do, P. (2021). Dy-
766 namic streaming potential coupling coefficient in porous media with different
767 pore size distributions. *Geophys. J. Int.*. doi: 10.1093/gji/ggab491
- 768 Thompson, A., & Gist, G. (1993). Geophysical applications of electrokinetic conver-
769 sion. *Lead. Edge*, *12*(12), 1169–1173.
- 770 Tyler, S. W., & Wheatcraft, S. W. (1990). Fractal processes in soil water retention.
771 *Water Resour. Res.*, *26*(5), 1047–1054.
- 772 Van Genuchten, M. T. (1980). A closed-form equation for predicting the hydraulic
773 conductivity of unsaturated soils. *Soil. Sci. Soc. Am. J.*, *44*(5), 892–898.
- 774 Wang, J., Hu, H., & Guan, W. (2015). Experimental measurements of seismoelectric
775 signals in borehole models. *Geophys. J. Int.*, *203*(3), 1937–1945.
- 776 Warden, S., Garambois, S., Jouniaux, L., Brito, D., Sailhac, P., & Bordes, C. (2013).
777 Seismoelectric wave propagation numerical modelling in partially saturated
778 materials. *Geophys. J. Int.*, *194*(3), 1498–1513.
- 779 Waxman, M. H., & Smits, L. (1968). Electrical conductivities in oil-bearing shaly
780 sands. *Soc. Pet. Eng. J.*, *8*(02), 107–122.
- 781 Yu, B., Li, J., Li, Z., & Zou, M. (2003). Permeabilities of unsaturated fractal porous
782 media. *Int. J. Multiph. Flow*, *29*(10), 1625–1642.
- 783 Zhou, M.-Y., & Sheng, P. (1989). First-principles calculations of dynamic permeabil-
784 ity in porous media. *Phys. Rev. B*, *39*(16), 12027.
- 785 Zhu, Z., & Toksoz, M. N. (2013). Experimental measurements of the streaming po-
786 tential and seismoelectric conversion in berea sandstone. *Geophys. Prospect.*,
787 *61*, 688-700.
- 788 Zhu, Z., Toksöz, M. N., & Burns, D. R. (2008). Electro seismic and seismoelectric
789 measurements of rock samples in a water tank. *Geophysics*, *73*(5), E153-E164.
790 doi: 10.1190/1.2952570
- 791 Zyserman, F. I., Jouniaux, L., Warden, S., & Garambois, S. (2015). Borehole seis-
792 moelectric logging using a shear-wave source: possible application to CO₂
793 disposal? *Int. J. Greenh. Gas Control.*, *33*, 89–102.
- 794 Zyserman, F. I., Monachesi, L. B., & Jouniaux, L. (2017). Dependence of shear

795 wave seismoelectrics on soil textures: a numerical study in the vadose zone.
796 *Geophys. J. Int.*, 208(2), 918–935.